ADVANCES IN ATMOSPHERIC SCIENCES, VOL. 32, JULY 2015, 979–990

Inter-comparison of the Infrared Channels of the Meteorological Imager Onboard COMS and Hyperspectral IASI Data

Dohyeong KIM[1], Myoung-Hwan AHN*[2], and Minjin CHOI[1]

[1]*National Meteorological Satellite Center of the Korea Meteorological Administration,* 64-18 *Guam-gil, Gwanghyewon-myeon, Jincheon-gun, Chungcheongbuk-do,* 365-830, *Republic of Korea*

[2]*Department of Atmospheric Science and Engineering, Ewha Womans University, 52 Ewhayeodae-gil, Seodaemun-gu, Seoul,* 120-750, *Republic of Korea*

(Received 13 June 2014; revised 30 September 2014; accepted 20 November 2014)

ABSTRACT

The successful launch and commissioning of the first geostationary meteorological satellite of Korea has the potential to enhance earth observation capability over the Asia Pacific region. Although the specifications of the payload, the meteorological imager (MI), have been verified during both ground and in-orbit tests, there is the possibility of variation and/or degradation of data quality due to many different reasons, such as the accumulation of contaminants, the aging of instrument components, and unexpected external disturbance. Thus, for better utilization of MI data, it is imperative to continuously monitor and maintain the data quality. As a part of such activity, this study presents an inter-calibration, based on the Global Space-based Inter-Calibration System (GSICS), between the MI data and the high quality hyperspectral data from the Infrared Atmospheric Sounding Interferometer (IASI) of the Metop-A satellite. Both sets of data, acquired for three years from April 2011 to March 2014, are processed to prepare the matchup dataset, which is spatially collocated, temporally concurrent, angularly coincident, and spectrally comparable. The results show that the MI data are stable within the specifications and show no significant degradation during the study period. However, the water vapor channel shows a rather large bias value of -0.77 K, with a root-mean-square difference (RMSD) of around 1.1 K, which is thought to be due to the shift in the spectral response function. The shortwave channel shows a maximum RMSD of around 1.39 K, mainly due to the coarse digitization at the lower temperature. The inter-comparison results are re-checked through a sensitivity analysis with different sets of threshold values used for the matchup dataset. Based on this, we confirm that the overall quality of the MI data meets the user requirements and maintains the expected performance, although the water vapor channel requires further investigation.

Key words: meteorological imager, inter-comparison, instrument long-term stability, water vapor channel

Citation: Kim, D., M. H. Ahn, and M. Choi, 2015: Inter-comparison of the infrared channels of the meteorological imager onboard COMS and hyperspectral IASI data. *Adv. Atmos. Sci.*, **32**(7), 979–990, doi: 10.1007/s00376-014-4124-1.

1. Introduction

The meteorological imager (MI) onboard the Communication, Ocean, and Meteorological Satellite (COMS) of Korea was designed and manufactured to meet user-required specifications that were tested and verified through lengthy ground tests conducted before the launch of the satellite. All of the specifications were validated during the in-orbit test, which occurred just after the launch of the satellite (Kim and Ahn, 2014). However, there are always possibilities of variation or degradation in data quality after the commissioning of the satellite. This can happen due to many different reasons, such as accumulation of contaminants, degradation of optical and electrical parts, excessive direct exposure to the sun, and any unexpected external perturbations such as unusually strong solar activity. For a stable and long-term application of the observation data, continuous monitoring and maintenance of payload performance and data accuracy carry significant implications. To fulfill such a requirement, the MI operator, the National Meteorological Satellite Center of the Korea Meteorological Administration, has been conducting several important activities.

One such activity at the international level is the Global Space-based Inter-Calibration System (GSICS) program, which started in 2005 under the auspices of the World Meteorological Organization (WMO) and the Coordination Group for Meteorological Satellites (CGMS). The major goal of GSICS is to provide accurate satellite data through inter-comparison and monitoring of various meteorological instruments onboard many different spacecrafts. To achieve this goal, international cooperation has been emphasized and the activities are conducted via comprehensive calibrations such as payload monitoring, operation of inter-calibration, repro-

* Corresponding author: M. H. AHN
Email: terryahn65@ewha.ac.kr

cessing of calibration data to maintain data characteristics for weather forecasting, climate monitoring, and environmental applications (Wang et al., 2009; Goldberg et al., 2011; Hewison et al., 2013).

The core activity of GSICS is to conduct inter-comparisons of the meteorological sensors onboard operational meteorological satellites (Goldberg et al., 2011; Hewison et al., 2013). Currently, the GSICS program compares between the sensors onboard the low-earth orbiter and geostationary orbiter satellites, and among the low-earth orbiter satellites themselves. The participating organizations for the geostationary sensors are required to use the GSICS recommended method with the recommended sensors onboard the low-earth orbiters (Hewison et al., 2013). For this, GSICS selected two sensors that have relatively high spatial resolution and with sufficiently high radiometric accuracies for the infrared channels. One is the Atmospheric Infrared Sounder (AIRS) onboard National Aeronautics and Space Administration (NASA)'s polar orbiting Aqua satellite, and the other is the Infrared Atmospheric Sounding Interferometer (IASI) onboard the EUMETSAT's operational polar orbiting weather satellite, Metop-A (Meteorology Operational Polar Satellite-A). As an IASI is also onboard Metop-B, the follow-on mission of Metop-A, and will be used for the whole first generation polar orbiters of EUMETSAT, it will play a significant role as a reference instrument during the lifetime of the MI. For the visible sensors, the Moderate Resolution Imaging Spectroradiometer (MODIS) onboard both the Terra and Aqua satellite is recommended.

In this paper, we report the long-term characteristics of the MI infrared channels for the first time, through the application of the GSICS concepts using three years of data. For a successful direct inter-comparison, one of the most important prerequisites is having a good matchup dataset. Here, we try to follow the basic requirements for the preparation of the matchup dataset, i.e. viewing the same target at the same time with the same viewing angle and having the same spectral response characteristics. However, in practice, it is hard for the two datasets to meet these conditions exactly. Thus, we apply a set of threshold values for the matchup conditions, while trying to follow the GSICS approaches (Wu et al., 2009; Hewison et al., 2013). In section 2, we briefly introduce the MI and describe the data used for the inter-comparison, followed by a brief description of the procedures to prepare the matchup dataset. The comparison results in the form of statistical parameters such as bias and root-mean-square difference (RMSD) as a function of several key parameters such as observation time and target temperature are presented in section 3. Results from a sensitivity study for the different sets of the threshold values used for the matchup dataset are also summarized in section 3. The paper is summarized and plans for future work are described in section 4.

2. Matchup dataset

The main purpose of inter-comparison is the quantification of the difference between the monitoring data and the reference data. With the derived quantification, we try to understand the causes of the difference with the ultimate goal of bias correction. Thus, for a proper inter-comparison, it is important to remove those factors that can introduce differences in the radiometric outputs other than factors caused by the differences in the instrument's characteristics. However, as having a perfectly matched dataset is impractical, a certain range of criteria is applied in the selection of the matchup dataset. The criteria are selected to produce a matchup dataset to have several characteristics. For example, we need to have sufficient data to acquire meaningful statistical parameters. Also, it is expected to have a sufficient range of the measured radiances that could encompass all of the observational situations, such as clear, cloudy, extremely dry or humid, or various types of surfaces. Finally, for the spatial size of the matchup data, it should be sufficiently large to mitigate any possible non-uniformity of the scene, but should be sufficiently small to prevent an excessive average that could mask the real signal (Wu et al., 2009; Hewison et al., 2013).

2.1. *Data*

The COMS satellite is Korea's first geostationary multi-purpose satellite with the capability of earth observation. The satellite was launched on 27 June 2010 into a transition orbit, and then moved into an operational orbit of 128.2°E. After about 8 months of successful in-orbit testing, the satellite began operational service on 1 April 2011 (Kim and Ahn, 2014). The main payloads of COMS are a Ka-band communication payload, an ocean color imager, and the MI. The first geostationary ocean color imager, called GOCI, has eight visible channels with 0.5-km spatial resolution at the satellite nadir point, and has a temporal resolution of one hour for an area of 2500 $\times$2500 km^2 centered on the Korean peninsula (Choi et al., 2012; Ryu et al., 2012).

In terms of the MI, the main payload for the meteorological mission, it has one visible channel and four infrared channels with a spatial resolution of 1 km and 4 km, respectively, at the satellite nadir point. Table 1 summarizes the specifications of each channel, including the center wavelength, dynamic range, and the required noise performances. Interestingly, the shortwave infrared (SWIR) channel has a different dynamic range; the high end is at 350 K compared to 330 K for the other channels. This value was purposefully selected to prevent saturation of the detector and thus to be able to detect a hot spot such as a forest fire. However, it should be noted that both the increased dynamic range and the radiation sensitivity result in a significant increase of noise equivalent delta temperature (NEdT) at lower temperature. On the other hand, the other three channels, water vapor (WV) and two infrared windows (IR1 and IR2), have a similar dynamic range and noise specifications, with larger NEdT values at lower temperature. The spectral response functions (SRFs) of the COMS MI imagers are shown in Fig. 1.

The reference data are from the IASI onboard Metop-A, the polar orbiters with an equator crossing time of 0930 LST at an altitude of about 840 km above the ground (the period is about 102 minutes). The Michelson type interfer-

Table 1. The specification of the COMS MI channels. The SNR (Signal-to-noise ratio) and NEdT (noise equivalent delta temperature) represented by albedo (at 100% and 5%) and temperature (at 300 K and 220 K).

Channel (range)	Center wavelength	Spatial resolution	Dynamic Range	SNR (VIS) or NEdT (IR)	
Visible (0.55–0.8 μm)	0.675 μm	1 km	0%–115% Albedo	170:1 @ 100% albedo	10:1 @ 5% albedo
SWIR (3.5–4.0 μm)	3.75 μm	4 km	110–350 K	0.10 K @ 300 K	5.7 K @ 220 K
WV (6.5–7.0 μm)	6.75 μm	4 km	110–330 K	0.12 K @ 300 K	0.58 K @ 220 K
IR1 (10.3–11.3 μm)	10.8 μm	4 km	110–330 K	0.12 K @ 300 K	0.40 K @ 220 K
IR2 (11.5–12.5 μm)	12.0 μm	4 km	110–330 K	0.20 K @ 300 K	0.53 K @ 220 K

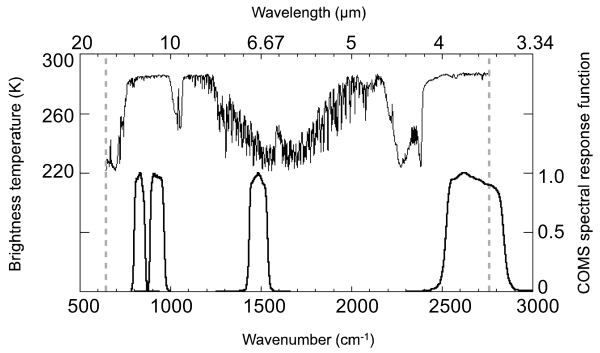

Fig. 1. IASI T_b spectra calculated from the MODTRAN overlaid with the SRFs from the COMS MI imagers.

ometer, IASI, covers the spectral ranges of 3.6–15.5 μm with 8461 channels for the spectral resolution of 0.5 cm^{-1} after apodisation (L1c spectra) with the spectral sampling interval of 0.25 cm^{-1} (Hilton et al., 2012; EUMETSAT, 2013). The radiometric accuracy of IASI data is known to be within 0.1 K, based on inter-comparison with AATSR (the Advanced Along Track Scanning Radiometer) and AIRS (Illingworth et al., 2009; Wang et al., 2010, 2011), which is the main reason for our choice as the reference data. With a spatial resolution of 12 km at nadir, the IASI data can provide information on the vertical distribution of temperature and humidity with an accuracy of 1 K km^{-1} and 10%, respectively. Also, with the high resolution hyper-spectral data, other geophysical parameters such as skin temperature and infrared emissivity, cloud top temperature and pressure, concentrations of trace gases including O_3, N_2O, CO, CO_2, and CH_4, are derived (Hilton et al., 2012).

To obtain sufficient comparison data, we use data obtained from April 2011 to March 2014, lasting about 36 months, when both MI and IASI data are available. The brightness temperature (T_b) used to describe the inter-comparison results is obtained by inverting the level 1B radiance data. The inversion temperature calculated by the Planck function at the center wavelength can be linearly fitted to obtain the broadband T_b of each channel. Here, the level 1B data are obtained after application of the operational radiometric calibration, followed by the image navigation and registration (INR) process, which is directly broadcasted through the antenna system of COMS. Two important limitations regarding the matchup dataset should be noted. First, although the MI covers a full disk area, its observation schedules are heavily in the so-called enhanced Northern Hemisphere area, by taking images every 15 minutes compared to the 3 hourly full-disk observation. Thus, the matchup dataset consists of a large portion of data from that area, which might not represent a full range of the observational conditions. This will be checked during the inter-comparison process. Second, the SWIR channel is affected by the reflected solar radiation that takes place during the daytime. Thus, the measured T_b is highly dependent on the target inhomogeneity, such as the cloud presence, and is complicated by the complex nature of the inhomogenity. To mitigate uncertainty caused by the target uncertainty, only the nighttime data for the SWIR channel are included in the matchup dataset.

2.2. *Procedures*

The first process is to make sure that the two instruments measure the signal coming from the same target at the same time. For this, we select MI data located nearby IASI data by using the IASI pixel position. To mitigate the effects caused by the pixel size difference between the MI and IASI (4 km vs 12 km at the sub-satellite point), we select the 3×3 MI instantaneous field-of-view (IFOV) to be collocated, referred to as the target pixels. In doing so, to reduce the effect of much faster increases in GEO (geosynchronous orbits) pixel size than IASI pixel size when the GEO scan angle increases, the scan angles of the GEO imager are limited by 40°, which corresponds to the 35°S–35°N/110°–160°E latitude/longitude range. We then select MI data obtained at the same time as IASI data by limiting the time difference to be less than 5 minutes, which is sufficiently long for enough collocation data and safely short for limiting a significant target change (Wu et al., 2009).

After selecting data that have the same target, we further check the observation geometry to ensure that the air mass is not significantly different for the two instruments. This is especially important for the channels that have a large atmospheric opacity, such as the WV channel of the MI. Although the air mass conditions of the two instruments generally include zenith, azimuth angle and so on, the difference could be checked with a simple comparison of zenith angles in the case of the GSICS intercomaprison of GEO and LEO (Low Earth Orbits). Here, we use a simple equation,

$$\left| \frac{\cos\theta_{\mathrm{MI}}}{\cos\theta_{\mathrm{IASI}}} - 1 \right| < \varepsilon_1, \tag{1}$$

where θ_{MI} and θ_{IASI} are the zenith angles of the MI and IASI at the given IFOV, respectively, and ε_1 is the threshold value of the test. Depending on the selected threshold value, the

characteristics of the mathcup dataset, and thus the comparison results, could be different. For example, too small a threshold would result in a smaller dataset, which could increase the statistical uncertainty. On the other hand, if ε_1 is too relaxed, the resulting data with large discrepancy could corrupt the statistical parameters. Thus, it is important to select an appropriate threshold value. Here, we choose 0.03 for all channels, which corresponds to the 3% difference in the air mass factor. In terms of angles, it corresponds to about 14° at the nadir (where the satellite zenith angle is close to 0°) and about 2° at the outer boundary (where the satellite zenith angle is 40°). To ensure that the threshold selection does not mislead the overall inter-comparison results, we perform sensitivity tests (section 3.2).

The geometry test introduces an additional consideration to be taken into account. With the increasing θ_{MI}, the corresponding θ_{IASI} also increases, resulting in an increase of the ground pixel size. When the pixel size increases, it would also increase the possibility of scene heterogeneity, resulting in an increased possibility of disparate signal collection. If this effect is not properly treated, there would be geometry and target dependences in the comparison result. Thus, an additional test for scene uniformity is performed using the signal variability of an area that is large enough to account for the expected variation, caused by at least two uncertainties. The first is the uncertainty of the MI pixel location, which is due to several causes, including incorrect knowledge of the satellite location, perturbations on the satellite attitude, and variation of the instrument's alignment. For the MI operational system, the INR accuracy is estimated to be better than about 4 km (Woo et al., 2013). Another component to be considered is the temporal variation of the target itself. For example, during the 5 minutes used for the collocation criteria, atmospheric conditions such as the cloudiness could change. In general, this kind of change can happen with a maximum flow speed of about 33 m s^{-1}, which corresponds to about 10 km of movement during the 5 minutes time criteria. To take into account these uncertainties (the uncertainty associated with the INR uncertainty and the atmospheric movement of about 11 km, i.e. $\sqrt{4^2+10^2} \approx 11$), we select 9×9 pixels, which are larger than the 3×3 target pixels and are called environmental pixels. We then use the following formula to screen out non-uniform targets from the matchup dataset:

$$9x\left(\frac{R_{\mathrm{F}} - R_{\mathrm{E}}}{\sigma}\right) < \varepsilon_2 \ . \tag{2}$$

Here, R_{F} and R_{E} denote the averaged radiances in the target pixel and the environmental pixel, respectively, while σ is the standard deviation (STD) of radiance within the environmental pixel. The threshold value ε_2 used for the current study is 2 for all four channels. Also, to ensure that we select the target pixels from the not too inhomogeneous environment, another set of threshold values, ε_3, for the uniformity test of the environmental pixels (MI radiance data over a box of 9×9 pixels) are applied. With an increase in the value of the environmental uniformity (ε_3), the spread of the T_{b} difference becomes larger. We choose the value based on Tahara and Kato (2009) to select spatially homogeneous scenes, and the threshold values used are 1.65, 1.82, 0.311 and 0.0151 for IR1, IR2, WV and SWIR, respectively, where the difference is mainly to take account of the average radiance measured, the largest at IR1 and the smallest at SWIR. The threshold values correspond to a ratio of $\sim 1.7\%$ of the standard deviation to the mean of the COMS MI collocated pixels' radiance.

2.3. *Normalization of the spectral response function*

Once the temporal and geometric collocation is performed, we apply the normalization procedure to ensure that the radiances obtained with the different SRFs become a spectrally comparable dataset. For an ideal case, a convolution of the hyperspectral IASI data with the MI SRF for the given channel would be sufficient for the normalization procedure. However, due to the different characteristics of the spectral responses of the MI and IASI, the constraint method (Tahara and Kato, 2009), which essentially derives a new spectral weighting function (ω_i) for each MI channel, as shown in Eq. (3), is applied first:

$$\varphi_{\mathrm{MI}}(\nu) \approx \sum \omega_i \varphi_{\mathrm{IASI}}(\nu) \ . \tag{3}$$

Here, $\varphi_{\mathrm{MI}}(\nu)$ and $\varphi_{\mathrm{IASI}}(\nu)$ represent the known MI SRF and IASI SRF, respectively. Once the spectral weighting function is derived, the IASI radiance values are converted into the MI equivalent IASI radiances [$R_{\mathrm{MI}}(\nu)$] using Eq. (4),

$$R_{\mathrm{MI}}(\nu) = \frac{\sum_i \omega_i R_i}{\sum_i \omega_i} \ , \tag{4}$$

where i denotes the IASI channel number and R_i is the IASI radiance.

Finally, there are cases for the hyperspectral radiance that do not fully cover the spectral bandwidth of the broadband imaging channels. For the MI and IASI, the bandwidth of the SWIR channel is not fully covered by the IASI. For this channel, we interpolate the available IASI radiance data using the simulated radiance prepared for the whole IASI spectral range with eight different atmospheric profiles using Line-By-Line Radiative Transfer Model (LBLRTM) (Clough et al., 1995). Using the simulated spectral radiance and the measured IASI radiance, the relation between the measured and simulated radiance is established and used to reconstruct the gap spectral radiance (Tahara and Kato, 2009).

3. Results

We first describe the comparison results derived from the matchup dataset obtained by the application of the baseline threshold values as a function of different conditions, such as target temperature, viewing angle, and time. After the overall characterization of the MI data, we further test the comparison results with applications of the different threshold values.

3.1. *Baseline dataset*

Figure 2 shows the scatter plot between the MI T_{b} and the IASI T_{b} for the whole study period and Table 2 summarizes the statistical parameters. Overall, there is excellent

Table 2. Results of inter-calibration with the different values of the collocation threshold.

Channel	TIME	NUMBER	BIAS	RMSD	CORR	Intercept	Slope
IR1	Day	36052	0.23	0.69	1.000	3.34	0.99
	Night	37225	0.06	0.59	1.000	3.65	0.99
	All	73277	0.14	0.64	1.000	3.70	0.99
IR2	Day	40334	0.06	0.61	1.000	3.10	0.99
	Night	38156	−0.00	0.52	1.000	3.67	0.99
	All	78490	0.03	0.57	1.000	3.88	0.99
WV	Day	61759	−0.75	1.10	0.997	6.06	0.97
	Night	62769	−0.78	1.11	0.997	7.85	0.96
	All	124528	−0.77	1.11	0.997	6.77	0.97
SWIR	Night	27401	0.00	1.39	0.998	−3.91	1.01

agreement between the two instruments' data, although the comparison results depend highly on the channel. For example, all four channels show high correlation coefficients, although the WV channel shows a slightly smaller correlation coefficient of 0.997. In terms of bias, they are all satisfactory, showing better than required NEdT, except for two cases. First of all, the WV channel shows a large negative bias value of about −0.77 K. Also, as shown in Fig. 3, the bias depends on the target temperature. For example, there is a large negative bias of about −1 K in a higher tab, which represents the clear-sky conditions. On the other hand, there is a positive bias of about 1 K in a lower tab, which is mainly obtained in cloudy conditions. Based on the work of Wu and Yu (2013), these kinds of temperature-dependent bias characteristics are caused mainly by the uncertainty in the SRF of the specific channel, effectively represented by the uncertainty in the center wavelength of the SRF. To derive the exact number for the SRF shift, further considerations such as the re-calibration of raw MI data along with the adjustment of derived IASI radiance are required, which are under investigation and will be reported in another paper. Another noticeable bias characteristic is shown in the daytime case of the IR1 channel; the difference between daytime and nighttime is about 0.17 K (0.06 K vs. 0.23 K), while it is about 0.06 K in the IR2 channel. On the other hand, there is no significant difference in the WV channel. The large difference in the window channel is further described later (refer Fig. 4). Finally, as for RMSD, the IR1 and IR2 channels show quite small values, less than about 0.7 K; and that of the WV chan-

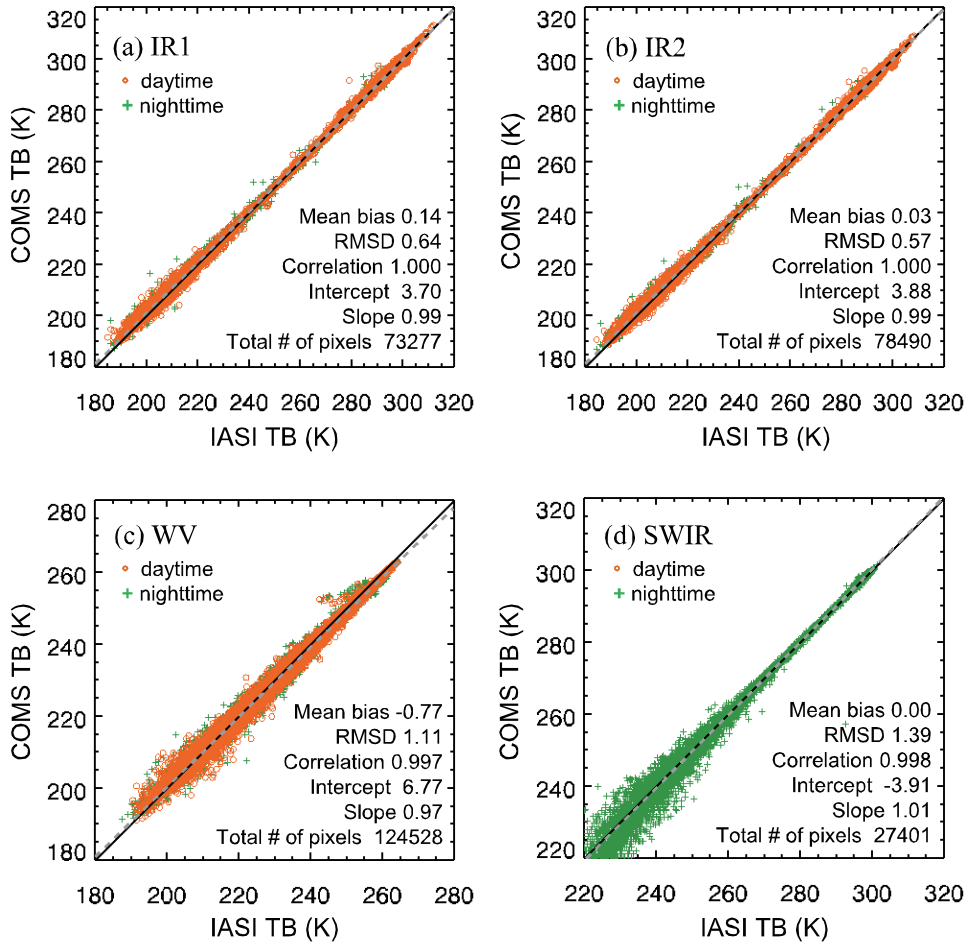

Fig. 2. Scatter plot of the collocated T_b from COMS/MI and Metop-A/IASI for the four MI infrared channels. All statistics given in the plot are calculated by all pixels including daytime and nighttime cases.

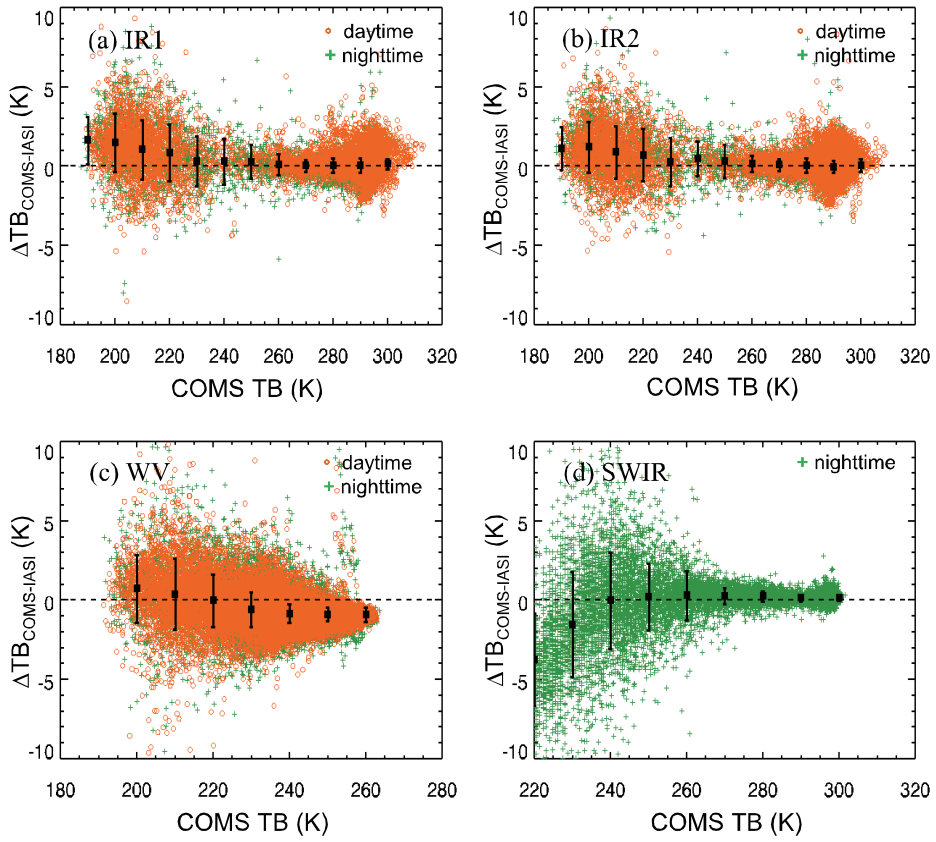

Fig. 3. The T_b difference between MI and IASI as a function of the MI T_b. Note the MI T_b range differs with channel.

nel is also close to 1 K, which is the calibration uncertainty of the MI (Kim and Ahn, 2014). However, the SWIR channel shows a much larger RMSD value of 1.39 K due mainly to the increased NEdT at the lower temperature. This demonstrates the high scatteredness and is described in more detail below.

As shown in Fig. 2, the T_b difference between the MI and IASI seemingly depends on the measured T_b. To characterize the difference with the measured T_b, Fig. 3 shows the T_b difference as a function of the MI T_b. Overall, the T_b difference is much smaller and stable at the higher MI T_b and increases with the cooler MI T_b. Bias and RMSD values of the IR1 and IR2 channels show quite a small value at the warm MI T_b, begin to increase at about 250 K, and show relatively large positive bias of about 1 K at the MI T_b of 200 K. This is explained by the fact that the IR channels are highly sensitive to the presence of cloud and its variability of properties such as optical depth. Thus, the sensitivity and NEdT of the IR channels increase with decreasing measured T_b, which is mainly caused by the presence of high clouds. It is most significant in the SWIR channel, which shows a sudden increase of variability starting from the MI T_b value of 260 K, and reaches a negative bias and large RMSD at the MI T_b of 230 K. The higher variability of the difference at the lower measured T_b in the SWIR channel has also been shown in other inter-comparison studies (Hewison et al., 2013; Wu et al., 2009). This can be caused by different sensitivities between T_b and the radiance, i.e. the T_b sensitivity against radiance increases significantly with decreasing radiance in the SWIR region. Another plausible cause is due to the wide spectral range compensation in addition to the relatively large noise of IASI radiances around the SWIR channel. This effect is exaggerated in the SWIR channel of the MI due to the increased dynamic range, as described before. On the other hand, the WV channel shows quite different characteristics. The bias shows a rather large negative value at the warm MI T_b, while it slowly increases with increasing MI T_b and reverses to a positive value at the coldest MI T_b. The RMSD value also shows a strong MI T_b dependence, being larger at the cooler MI T_b, which is primarily related with the systematic bias of the MI T_b.

The optical path length to the instrument onboard the satellite changes greatly with the observation geometry, thus affecting the measured radiances. Therefore, it is interesting to check whether the simple threshold test applied for the viewing geometry results in any significant residual effects in the comparision results. For this, the T_b differences as a function of the MI zenith angle are shown in Fig. 4. At first glance, there seems to be no significant variation in the MI zenith angle for all four channels. However, closer inspection reveals that bias and STD are worst near the nadir and improve with increasing zenith angle. For example, in the SWIR channel where the variation is most prominent, bias (STD) is -0.35 (3.5) K at the MI zenigh angle of 10°, while

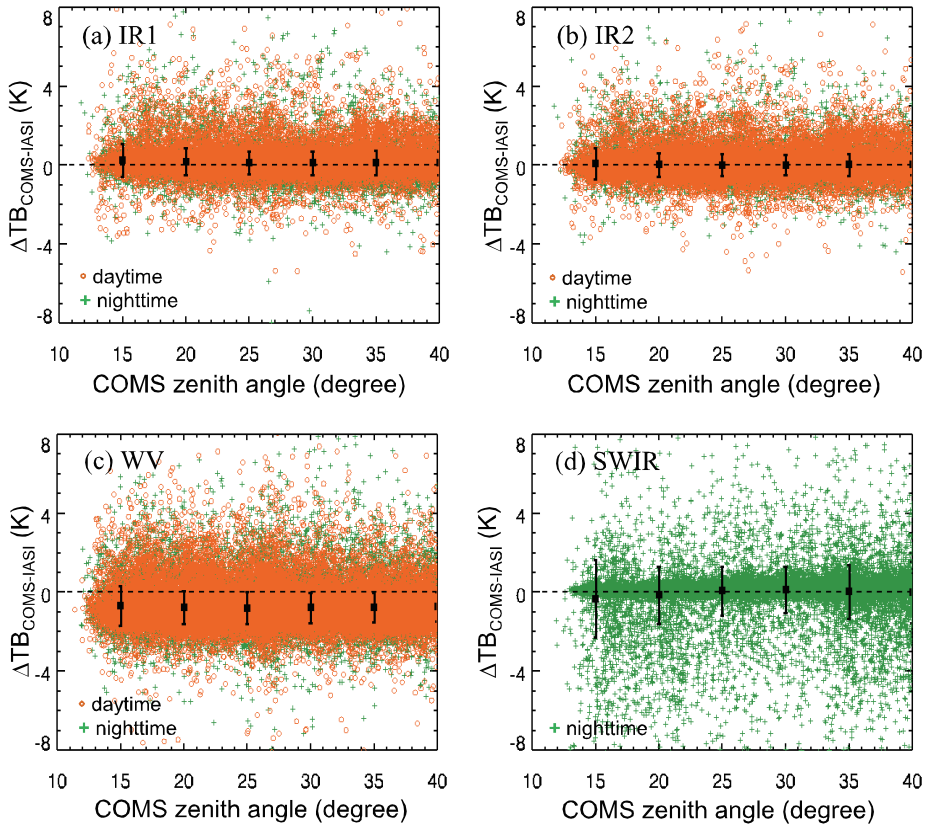

Fig. 4. The T_b difference between MI and IASI as a function of the MI satellite zenith angle.

it is 0.12 (2.7) K and 0.00 (2.4) K at 25° and 35°, respectively. The slight improvement in the bias and STD toward the higher MI zenith angle is shown in all IR channels except the WV channel, which shows little variation. The zenith angle dependence is thought to be caused by the fact that the viewing angle difference is the largest at nadir and smallest at the scan edge. However, the overall variation of statistical parameters with MI zenith angle is much smaller than the calibration uncertainty of the MI; therefore, it is concluded that the simple threshold check does not introduce a significant residual.

Based on the monitoring results of legacy instruments, such as the imagers onboard the GOES (Geostationary Operational Environmental Satellite) series, the calibration coefficient and its stability show diurnal and seasonal variation (Weinreb and Han, 2003), due mainly to the relative geometry between the sun and satellite, which introduces the temperature variation of the instrument's optics. Thus, it is also imperative to check if there is any temporal variability in the measured T_b. For this, the inter-comparison results are given as a time series of monthly mean bias and RMSD in Figs. 5 and 6, respectively. There are several characteristics to be noted in the monthly mean values. First, it is clear that there is no significant long-term drift in both bias and RMSD for all channels. According to the RMSD, the overall performance is slightly better during the recent months compared to the early operation period.

Second, there is seasonal dependence in both bias and RMSD (weak in bias and rather prominent in RMSD) in all four channels. For example, RMSD is maximum during the summer, around July, and minimum around Feburary. The variation is largest in the SWIR channel, where it is most sensitive to the noise signal at lower T_b. This kind of seasonal dependence has also been shown in comparison results based on similar instruments onboard GOES-11 and MTSAT-2, although it is much weaker in the case of GOES-12 (Hewison et al., 2013, Figs. 9–11). The seasonal dependence is closely related to the variation of solar illumination angles, which results in an increase of the detector patch temperature and stronger optics variation, including internal blackbody, scan mirror etc. (Weinreb and Han, 2003).

The large day and night difference in bias during the summer months shown in Figs. 5 and 6 is closely related with that of the IR1 and IR2 channels in Table 2. During the early period of operation, say September 2011, the day and night difference in bias is as large as 0.8 K in the IR1 channel and about 0.4 K in the IR2 channel, while it is insignificant in the WV channel. One plausible explanation for the channel and seasonal dependency of the day and night difference is the increased skin temperature over the land mass during the daytime of the summer season. Then, any inhomogeneity or difference between the MI targets and IASI pixels could be amplified. However, the bias and RMSD derived from the ocean-only dataset shows only a slight improvement, 0.20 K vs 0.23 K, for the daytime in the IR1 channel, while there are no changes in the WV channel. Thus, the exact causes

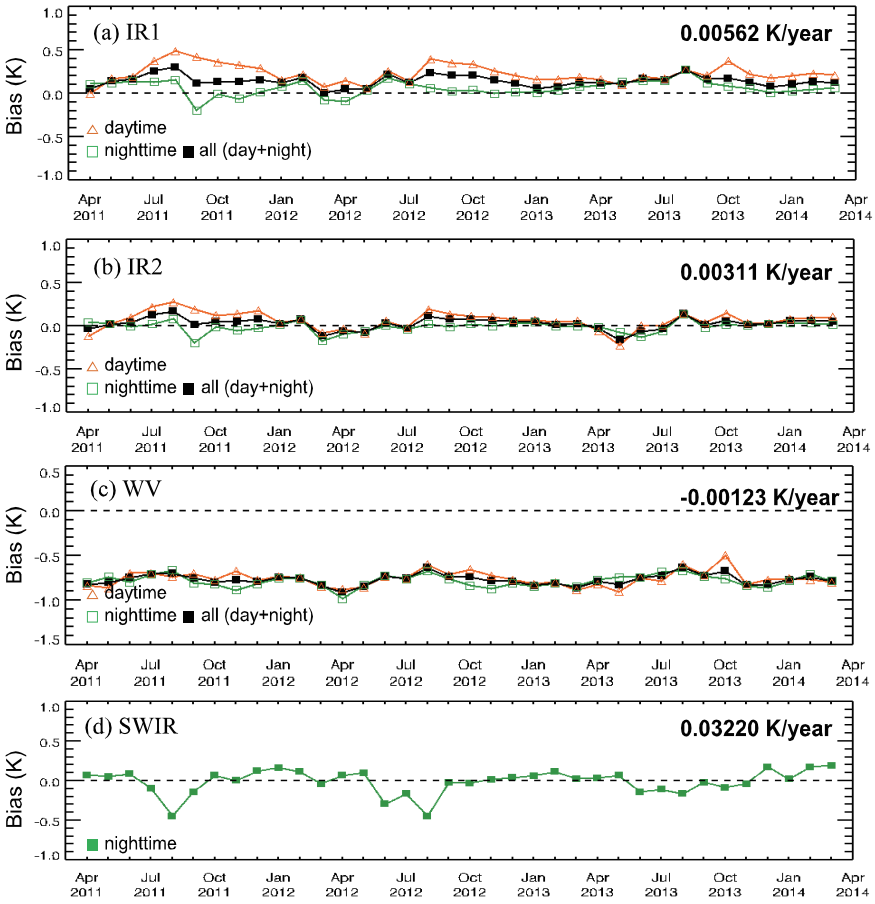

Fig. 5. Time series of monthly mean bias between MI T_b and IASI T_b for the four infrared channels.

of the rather large day and night difference, albeit which has gradually decreased since the commissioning of the satellite, remain to be solved.

Finally, the monthly mean bias for the WV channel shows a clear negative bias and its absolute magnitude is much larger than that of the other three channels. However, its seasonal variation is much weaker. This is also true for the RMSD, which shows a smooth variation but with comparatively smaller absolute values, near 1 K for all months. This kind of large negative mean bias shown in the MI is not apparent in the comparison results from either MTSAT-2 or the GOES series. MTSAT-2 shows a stable negative bias with much lower value (around −0.3 K), while the GOES series show positive and negative values, within 0.3 to 0.4 K (Hewison et al., 2013). Based on the stable RMSD and consistent bias trend with the comparison results from other satellites, we consider this characteristic is largely due to the uncertainty in the spectral response function, although it has not been solidly demonstrated (Wu and Yu, 2013).

3.2. *Sensitivity tests*

The threshold values used for the preparation of the matchup dataset are similar but slightly different from the previous GSICS activities (Tahara, 2008; Hewison et al., 2013). Although most of the participating organizations utilize the approaches and recommended threshold values, the specific process and threshold values could be modified to accommodate their own characteristics (Wu and Yu, 2011; Hewison et al., 2013). Thus, to perform a simple sensitivity test, we check the variability of the comparison results with the different sets of thresholds used for each criteria test. For simplicity, we vary the threshold values by halving and doubling them for the time and uniformity tests. For the viewing geometry, we apply an extremely small difference of 0.003 and a moderately small difference of 0.01, which is the value recommended for all conditions if the number of data is not a significant issue (Wu and Yu, 2011). A total of eight different cases are selected and the combinations of the different threshold values are summarized in Table 3.

Table 4 summarizes the variation of the statistical parameters with the different sets of the threshold values applied to all-day data (the variability characteristics for day and night are almost the same; thus, we show only the results from all-day data), and Fig. 7 shows the scatter plot of the MI T_b and the IASI T_b of the IR1 channel for the different cases. First, the utilization of a 1 minute temporal threshold value (Case I) reduces the number of matchup data by about 80%, with a slight improvement in bias and RMSD. When the threshold value is relaxed to 15 minutes (Case II), the data points increase more than tenfold, with a slight degradation of bias

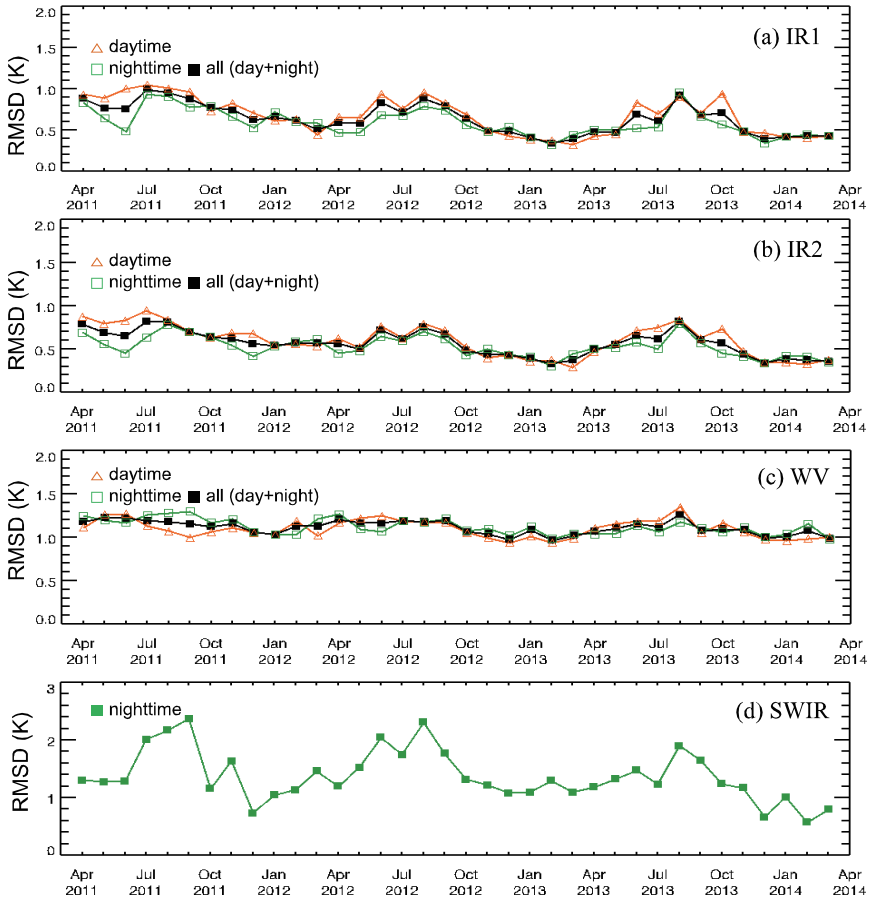

Fig. 6. As in Fig. 5 except for time series of monthly mean RMSD.

Table 3. Cases for the sensitivity test of the threshold values used for the preparation of the collocation dataset.

		Threshold values			
	Case	Time (s)	ε_1	ε_2	ε_3
Baseline		300	0.03	2	-
Temporal resolution	I	60	0.03	2	-
	II	900	0.03	2	-
Viewing geometry	III	300	0.01	2	-
	IV	300	0.003	2	-
Environmental uniformity	V	300	0.03	2	$\times 0.5$
	VI	300	0.03	2	$\times 2$
Radiance difference	VII	300	0.03	1	-
	VIII	300	0.03	4	-

and RMSD. Thus, unless there is a strong requirement for an increase of the matchup dataset, the 5 minute threshold looks a reasonable choice. For the viewing geometry, if the threshold value is reduced to 0.01, the available data points decrease to about one-third, with slight improvements in both bias and RMSD, especially in the SWIR channel. Even with the threshold value of 0.003, the improvements in bias and RMSD are not that impressive, although the number of data points is reduced to about one-tenth. Thus, it turns out that the error statistics are not very sensitive to the threshold values for the temporal and viewing geometry and the current threshold values provide a reasonable number of data points and error statistics.

On the other hand, when we tighten the uniformity constraint by twofold (Case V), the bias and RMSD show significant variation, with data reduction of about 40%. In the IR1 channel, both bias and RMSD improve by 0.03 K and 0.22 K, respectively. The IR2 channel shows similar improvement. However, the SWIR channel shows an opposite result, i.e. bias and RMSD degrade by about 0.17 K and 0.09 K, respectively. In the case of the WV channel, bias is degraded slightly by 0.05 K, although the RMSD improves significantly, by 0.14 K. This might explain some of the MI T_b dependence of the RMSD of the WV channel shown in Fig. 4. Thus, with a tightened threshold value, the statistical parameters improve significantly, with the exception of the SWIR channel, which shows a significant degradation of bias and RMSD. On the other hand, when the constraint is relaxed by twofold (Case VI), then the statistical parameters, especially the RMSD, show clear degradation in all channels, by as much as 0.43 K for RMSD in the IR2 channel. Thus, the comparison results are sensitive to the threshold value used for the uniformity test and the responses are different for different channels and error parameters.

Finally, the threshold for the radiance difference between

Table 4. Variation of statistical parameters along with the number of data (#) for the sensitivity tests specified in Table 3.

			Temporal resoltuion		Viewing geometry		Environmental Uniformity		Radiance difference	
Channel	Parameter	Baseline	I	II	III	IV	V	VI	VII	VIII
IR1	BIAS	0.14	0.15	0.16	0.14	0.13	0.12	0.16	0.14	0.14
	RMSD	0.64	0.65	0.76	0.63	0.61	0.42	1.06	0.64	0.63
	R^2	1.000	1.000	0.999	1.000	1.000	1.000	0.999	1.000	1.000
	#	73277	14319	169026	24196	7202	41211	116372	36784	140610
IR2	BIAS	0.03	0.03	0.04	0.03	0.03	0.00	0.06	0.03	0.03
	RMSD	0.57	0.55	0.68	0.56	0.55	0.35	1.00	0.58	0.56
	R^2	1.000	1.000	1.000	1.000	1.000	1.000	0.999	1.000	1.000
	#	78490	15387	179772	26005	7786	44693	121329	39655	149143
WV	BIAS	−0.77	−0.77	−0.75	−0.76	−0.76	−0.82	−0.72	−0.76	−0.77
	RMSD	1.11	1.10	1.16	1.09	1.08	0.97	1.42	1.11	1.11
	R^2	0.997	0.997	0.996	0.997	0.997	0.998	0.994	0.997	0.997
	#	124528	25054	303265	40853	12215	90656	147054	64584	217417
SWIR	BIAS	0.00	0.05	−0.01	0.00	−0.03	−0.17	0.10	0.00	−0.03
	RMSD	1.39	1.28	1.63	1.37	1.40	1.48	1.60	1.39	1.43
	R^2	0.998	0.998	0.998	0.998	0.998	0.999	0.997	0.998	0.998
	#	27401	5323	63520	9087	2659	11971	49139	13975	52010

the target pixel and the environment pixel is varied by halving (Case VII) and doubling (Case VIII) the value. Overall, the number of data points varies linearly with the threshold value, although the bias and RMSD do not show any significant variation. The largest difference is seen for bias in the SWIR channel with the relaxed constraint, with the degradation being about 0.04 K. Thus, as found for other threshold values that are not changed, changing the threshold value for the radiance difference does not produce significant variation in the comparison results.

From the simple sensitivity test, we can draw several conclusions. First, the comparison results are significantly sensitive to the changes in the threshold values for the environment uniformity test, especially a large change in RMSD. However, the sensitivity also depends on the channel, which suggests it is wise to use different sets of threshold values for different channels, if more detailed analysis for a certain channel is required. As a result, the changes in threshold values for other tests do not introduce significant variation in the comparison results and the baseline sets give quite representative numbers, which are comparable with the expected instrument performance (Kim and Ahn, 2014), and a similar inter-satellite comparison study (Kim et al., 2014).

4. Conclusion

4.1. *Summary*

For the first time, the overall performance of radiometric calibration for the four infrared channels of the MI onboard COMS is evaluated through inter-satellite comparison. For the evaluation, well-calibrated and high quality reference data from the hyperspectral sounding instrument, IASI, of the Metop satellite are used to prepare the matchup dataset to be spatially collocated, temporally concurrent, angularly coincident, and spectrally comparable. For this, we first search for MI data located with IASI data, and then select the data if the time difference is less than 5 minutes. To check the viewing geometry, optical path length is used and the difference should be smaller than 3%. For the current study, the cloudy pixels are also included to extend the comparison range of the measured T_b. To mitigate the effects due to the scene variability and pixel size difference, the scene uniformity is checked by two tests: the uniformity of environmental pixels and the radiance difference between the target pixel and the environmental pixel. By limiting the radiance difference within the variability of the environmental pixel, we ensure that the target is representative of the larger area (Wu et al., 2009; Hewison et al., 2013). Also, by limiting the variability of the environmental pixel, we can exclude a target pixel selected from a scene that has a large spatial inhomogeneity. Finally, the collocated data are further processed to be spectrally consistent by applying the constrained approach.

During the three years of the study period, more than 70 000 of matched data points are prepared and the overall comparison results are quite satisfactory. The bias is within the specification, although there is a large negative bias of about 0.77 K in the WV channel, which is thought to be due to the uncertainty in the spectral response function. The SWIR channel shows the largest RMSD value of about 1.4 K, while the other three channels show around 1 K or smaller RMSD with less variability. The comparison results are not very sensitive to the different observation conditions, although there are unresolved issues such as the difference in the bias and RMSD between day and night in the two window channels, IR1 and IR2. Another issue remained to be solved is that the difference is more prominent during the early period of operation with the gradual decrease. The noise signal is quite small, as expected with the lower patch temperature, although the large negative bias is not seen in the post-launch test (Kim and Ahn, 2014).

To check the reliability of the statistical parameters, we

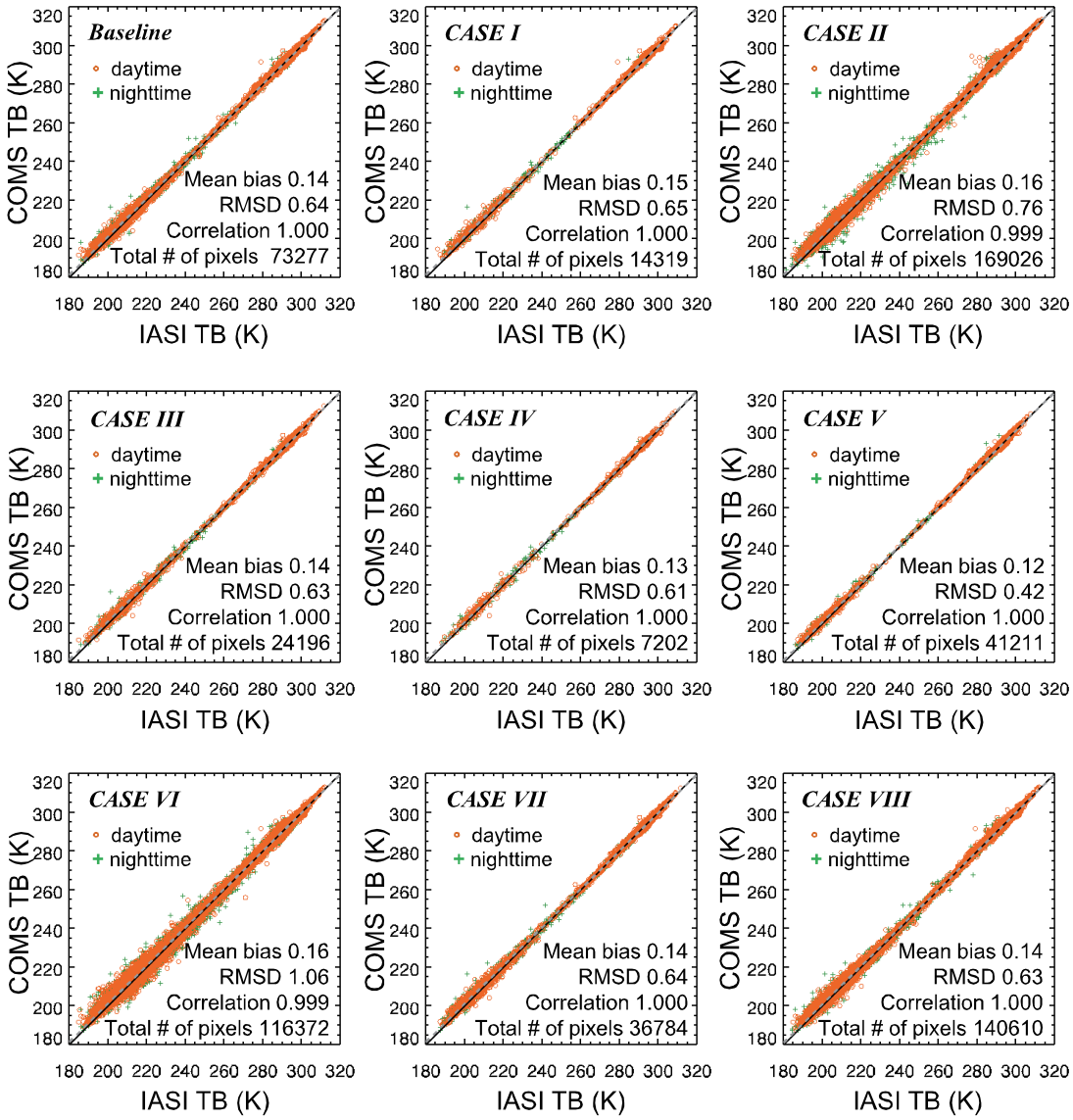

Fig. 7. Scatter plot of the MI T_b and the IASI T_b of the IR1 channel for different combinations of threshold values applied in the collocation tests. Each case is given in Table 3. All statistics given in the plot are calculated by all pixels including daytime and nighttime cases.

conduct a simple sensitivity test with the different sets of threshold values used for the matchup dataset. Based on the results, the statistical parameters are significantly sensitive to the threshold value used for the uniformity test of the environmental pixels, at least in the IR1, IR2 and WV channels. However, the resulting statistical parameters with the stricter threshold values are comparable with the baseline threshold values. Therefore, unless required for a specific purpose with a sufficient number of available data, baseline threshold values could be used for inter-comparison. On the other hand, the statistical parameters are not very sensitive to the other threshold values used for the tests, such as the temporal consistency, viewing geometry, and radiance difference between the target pixels and environmental pixels. The conclusions derived from the inter-comparison are not very sensitive to the different sets of threshold values.

4.2. *Discussion*

A previous study by Kim et al. (2014), using MODIS data as a reference instrument with the limited data period from January 2011 to April 2011, also shows a quite reliable comparison result. Although overall the characteristics are quite similar, the large negative bias shown in the WV channel does not show up in the MODIS comparison (Kim et al., 2013, Fig. 6). Rather, their results show a large negative bias in the IR1 channel, as large as -0.79 K, with much smaller RMSD, less than 0.4 K, in all four channels except the WV channel, where the RMSD value is as much as 0.8 K. The different comparison characteristics could be due to the difference in the reference instrument (the much higher spatial

resolution with different spectral characteristics of MODIS), in the collocation approach (uniformity test used within the selected FOV instead of the environment FOV), the different criteria for the viewing angle (difference should be less than 5°), and the collocation pixel size ($0.2° \times 0.2°$). Furthermore, the study period was much shorter (4 months vs 36 months), and the compared MI data were obtained before commissioning. However, it would be quite informative if the comparison with MODIS is extended to the same period as in the current study. Also, it is imperative to further investigate the root cause of the large negative bias shown in the WV channel, especially given that this channel is important in several applications, including not only synoptic analysis, but also quantitative value-added products such as the derivation of cloud top altitude and the detection of overshooting clouds.

Acknowledgements. The work was supported by the project entitled "Development of Meteorological Satellite Operation and Application Technology" of the KMA/NMSC (Korea Meteorological Adminstration/National Meteorological Satellite Center). M. H. AHN is partially supported by the Eco Innovation Program of KEITI (Korea Environmental Industry & Technology Institute) (Grant No. 2013000160002).

REFERENCES

Choi, J.-K., Y. J. Park, J. H. Ahn, H. S. Lim, J. Eom, and J.-H. Ryu, 2012: GOCI, the world's first geostationary ocean color observation satellite, for the monitoring of temporal variability in coastal water turbidity. *J. Geophys. Res.*, **117**(C9), doi: 10.1029/2012JC008046.

Clough, S. A., M. W. Shephard, E. J. Mlawer, J. S. Delamere, M. J. Iacono, K. Cady-Pereira, S. Boukabara, and P. D. Brown, 2005: Atmospheric radiative transfer modeling: A summary of the AER codes. *Journal of Quantitative Spectroscopy and Radiative Transfer*, **91**, 233–244.

EUMETSAT, 2013: IASI Level 1 Products Guide. EUM/OPS-EPS/MAN/04/0032, v4A, EUMETSAT, Darmstadt, Germany. [Available online at http://oiswww.eumetsat.org/WEBOPS/eps-pg/IASI-L1/IASIL1-PG-0TOC.htm.]

Goldberg, M., and Coauthors, 2011: The global space-based intercalibration system (GSICS). *Bull. Amer. Meteor. Soc.*, **92**(4), 468–475.

Hewison, T. J., X. Wu, F. Yu, Y. Tahara, X. Hu, D. Kim, and M. König, 2013: GSICS inter-calibration of infrared channels of geostationary imagers using Metop/IASI. *IEEE Trans. Geosci. Remote Sens.*, **51**(3), 1160–1170.

Hilton, F. I., and Coauthors, 2012: Hyperspectral earth observation from IASI: Five years of accomplishments. *Bull. Amer. Meteor. Soc.*, **93**(4), 347–370.

Illingworth, S. M., J. J. Remedios, and R. J. Parker, 2009: Inter-comparison of integrated IASI and AATSR calibrated radiances at 11 μm and 12 μm, IASI data. *Atmos. Chem. Phys.*, **9**, 6677–6683.

Kim, B.-R., S.-H. Ham, D. Kim, and B. J. Sohn, 2014: Post-Flight radiometric calibration of the Korean geostationary satellite COMS meteorological imager. *Asia-Pac. J. Atmos. Sci.*, **50**(2), 201–210, doi: 10.1007/s13143-014-0008-7.

Kim, D., and M. H. Ahn, 2014: Introduction to the in-orbit-test and its performance of the first meteorological imager of the Communication, Ocean, and Meteorological Satellite. *Atmos. Meas. Tech.*, **7**, 2471–2485, doi: 10.5194/amt-7-2471-2014.

Ryu, J. H., H. J. Han, S. Cho, Y. J. Park, and Y. H. Ahn, 2012: Overview of geostationary ocean color imager (GOCI) and GOCI data processing system (GDPS). *Ocean Science Journal*, **47**(3), 223–233.

Tahara, Y., 2008: New approach to intercalibration using high spectral resolution sounder, MSC/JMA Technical Note, No. 50, 1–14.

Tahara, Y., and K. Kato, 2009: New spectral compensation method for intercalibration using high spectral resolution sounder. MSC/JMA Technical Note, No. 52, 1–37.

Wang, L., C. Cao, and M. D. Goldberg, 2009: Intercalibration of GOES-11 and GOES-12 water vapor channels with MetOp/IASI hyperspectral measurements. *J. Atmos. Oceanic Technol.*, **26**, 1843–1855.

Wang, L. K., X. Q. Wu, M. Goldberg, C. Y. Cao, Y. P. Li, and S. H. Sohn, 2010: Comparison of AIRS and IASI radiances using GOES imagers as transfer radiometers toward climate data records. *J. Appl. Meteor. Climatol.*, **49**, 478–492.

Wang, L. K., M. Goldberg, X. Q. Wu, C. Y. Cao, R. A. Iacovazzi Jr., F. F. Yu, and Y. P. Li, 2011: Consistency assessment of atmospheric infrared sounder and infrared atmospheric sounding interferometer radiances: Double differences versus simultaneous nadir overpasses. *J. Geophys. Res.*, **116**, D11111, doi: 10.1029/2010JD014988.

Weinreb, M., and D. Han, 2003: Implementation of midnight blackbody calibration correction (MBCC). NOAA NESDIS Office of Satellite Operations. [Available online at http://www.ospo.noaa.gov/Operations/GOES/calibration/mbcc_implemmentation.html.]

Woo, J., B. I. Lee, H. Oh, J. S. Kim, and S. H. Sohn, 2013: Diurnal variation of COMS MI image navigation and registration performance. 4*th Asia-Oceania Meteorological Satellite Users Confereence*, Oct. 9–11, Melbourne, Australia.

Wu, X., and F. Yu, 2011: GSICS Algorithm Theoretical Basis Document (ATBD) for GOES-AIRS/IASI Inter-Calibration, NOAA NESDIS. [Available online at https://gsics.nesdis.noaa.gov/wiki/GPRC/AtbdCentral.]

Wu, X. Q., and F. F. Yu, 2013: Correction for GOES imager spectral response function using GSICS. Part I: Theory. *IEEE Trans. Geosci. Remote Sens.*, **51**(3), 1215–1223.

Wu, X. Q., T. Hewison, and Y. Tahara, 2009: GSICS GEO-LEO inter-calibration: Baseline algorithm and early results. *Proc. SPIE*, **7456**, 745604-1–745604-12.